A Depth Semi-Averaged model for coastal dynamics

M. Antuono,[1,2,a)] G. Colicchio,[1,2] C. Lugni,[1,2] M. Greco,[1,2] and M. Brocchini[3]

[1)] *CNR-INSEAN, Marine Technology Centre, Rome, Italy*

[2)] *AMOS, NTNU, Dept. of Marine Technology, Trondheim, Norway*

[3)] *Università Politecnica delle Marche, Ancona, Italy*

(Dated: 16 December 2016)

The present work represents the research continuation on the semi-integrated method proposed by Antuono and Brocchini [1], this being composed by a subset of depth-averaged equations (like the popular Boussinesq-like models) and by a Poisson equation that accounts for the vertical dynamics. On the theoretical side, the subset of depth-averaged equations has been reshaped in a conservative-like form with inherent advantages when applied at the discrete level. On the numerical side, the Poisson equation has been inspected in both formulations proposed in Antuono and Brocchini [1]: a Poisson equation for the vertical component of the velocity (formulation A) and a Poisson equation for a specific depth semi-averaged variable, Υ (formulation B). The studies showed that formulation A is prone to instabilities as the problem nonlinearities increase. On the contrary, formulation B allows for an accurate and robust numerical implementation.

Some relevant test cases derived from the scientific literature on Boussinesq-type models - i.e. solitary and Stokes wave analytical solutions for linear dispersion and nonlinear evolution and experimental data for shoaling properties - have been used to assess the proposed solution strategy and to highlight its features and characteristics. The method proved to predict reliable results for wave solutions in shallow to intermediate waters, both in terms of semi-averaged variables and conservation properties.

PACS numbers: 47.35.Bb

Keywords: gravity waves, non-hydrostatic models, Boussinesq models, Stokes waves

[a)] Electronic mail: matteo.antuono@cnr.it

I. INTRODUCTION

In the continuous progress of research activity (see, for example, Lakatos[2]), the nearshore hydrodynamics moved from potential-type solvers to Nonlinear Shallow Water Equations and, then, to Boussinesq-type Equations (e.g. Peregrine[3], Brocchini[4]). However high-order expansions are needed to extend the validity range of Boussinesq-type models. This leads to: 1) complicated sets of equations that are difficult to be coded and used in the practice, 2) a description of the flow still based on one single representative velocity (e.g. Kirby[5]). This has motivated a further evolution from the fundamental Boussinesq-type modeling to the new grounds of hyperbolic-dispersive (e.g. Antuono et al.[6]) and non-hydrostatic calculations (e.g. Antuono and Brocchini[1], Kirby[5], Casulli and Stelling[7], Zijlema et al.[8], Ma et al.[9]). In particular, non-hydrostatic models, which take such name because the pressure field is not just the leading-order hydrostatic contribution, seem the most suitable to become, after Boussinesq-type models, the new tool of reference for the analysis of the nearshore hydrodynamics. In fact, these methods overcome the above limitations of Boussinesq-type models, since they retain the relative efficiency of depth-integrated solvers as well as providing access to a fully three-dimensional determination of flow characteristics.

In the non-hydrostatic model proposed by Antuono and Brocchini[1] the continuity and horizontal momentum equations are integrated over the depth, while information about the non-hydrostatic component of the pressure field leads to a Poisson equation for the vertical velocity component, which is then solved to obtain the 3D flow field for use in the integrated 2D continuity and momentum equations. The proposed method has not been implemented numerically to date, but it is potentially more efficient than the direct approach to the 3D problem used to date (e.g. Kirby[5]).

The present contribution aims at demonstrating that the non-hydrostatic model of Antuono and Brocchini[1] is, indeed, a powerful and efficient model for the description of the nearshore hydrodynamics, comprehensive of its vertical structure. To this aim, the model framework is recalled in section II, which also details the specific choice made in the solution of the Poisson's equation for the vertical flow dynamics. Section III describes the numerical implementation, with specific focus on the solution of the Poisson equation and, finally, a number of benchmarking calculations is proposed in section IV to illustrate the actual capabilities of the solver.

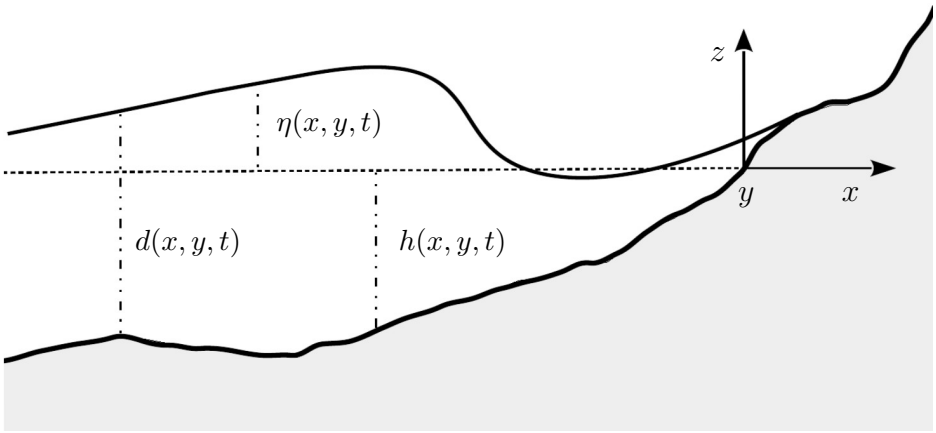

FIG. 1. Sketch of the geometry and of the frame of reference. The horizontal dashed line indicates the still water level.

II. THE DEPTH SEMI-AVERAGED MODEL

In the coastal-water framework, the wave motion is governed by two dimensionless parameters that account for wave nonlinearity and dispersive effects. These parameters are $\epsilon = H^*/h_0^*$ and $\mu = 2\pi h_0^*/L^*$, respectively. Here, h_0^* is the reference depth in still-water conditions, L^* is the characteristic wave length and H^* is the wave height. Accordingly, we use the following scaling, which is standard for Boussinesq-type modeling (e.g. Veeramony and Svendsen[10]):

$$
\begin{aligned}
&x^* = \frac{h_0^*}{\mu}\, x, \qquad y^* = \frac{h_0^*}{\mu}\, y, \qquad z^* = h_0^*\, z, \qquad t^* = \frac{1}{\mu}\sqrt{\frac{h_0^*}{g^*}}\, t,\\
&u^* = \epsilon\,\sqrt{g^* h_0^*}\, u, \quad v^* = \epsilon\,\sqrt{g^* h_0^*}\, v, \quad w^* = \epsilon\,\mu\,\sqrt{g^* h_0^*}\, w, \qquad h^* = h_0^*\, h,\\
&\eta^* = H^*\,\eta, \qquad p^* = \rho^*\, g^*\, H^*\, p, \quad \nu_T^* = \mu\, h_0^*\,\sqrt{g^* h_0^*}\,\nu_T, \quad \overline{\kappa}^* = \epsilon\,\mu^2\, g^*\, h_0^*\,\overline{\kappa}
\end{aligned}
\tag{1}
$$

and where the eddy viscosity, scaling with $\sqrt{g^* h_0^*}$ and h_0^* as $\nu_T^* \sim 0.03 h_0^* \sqrt{g^* h_0^*}$ (e.g. Cox et al.[11]), has been made dimensionless with an extra μ contribution as suggested by Veeramony and Svendsen[10]. Figure 1 displays a sketch of the beach bathymetry for a typical beach nearshore problem, as well as the main geometrical variables in use. The axes origin is posed at the undisturbed shoreline; the x-coordinate gives the onshore direction and points in the landward direction, the z-coordinate points upward, the tern (x, y, z) forming a right-handed Cartesian reference frame. The total water depth is $d = \epsilon\,\eta + h$ where η is the

free-surface elevation and $-h$ is the bottom seabed location.

The Depth Semi-Averaged model is obtained through a proper rearrangement of the Semi-Integrated model proposed by Antuono and Brocchini [1] (see the Appendix A for details). The main idea is to rewrite the original scheme in a conservative form, in order to take advantage of the copious theoretical and numerical results on systems of conservation laws available in the scientific literature. The details of computations are quite long and tedious and, therefore, are given in Appendix A. The resulting constitutive equations can be written in the following compact form:

$$\begin{cases} \dfrac{d_t}{\epsilon} \,+\, \nabla \cdot \boldsymbol{Q} \,=\, 0\,, \\[2ex] \boldsymbol{M}_t \,+\, \nabla \cdot \mathbb{F} \,=\, \left(d \,+\, \epsilon\, \mu^2 p_b \,+\, \mu^2\, p_b^T \right)\, \nabla h \,+\, \boldsymbol{\tau}_b\,, \\[2ex] \mu^2\, \Upsilon_{xx} \,+\, \mu^2\, \Upsilon_{yy} \,+\, \Upsilon_{zz} \,=\, \nabla \cdot \left(\dfrac{\boldsymbol{M}}{d} + \boldsymbol{R} \right), \end{cases} \tag{2}$$

where $\nabla \,=\, (\partial/\partial x, \partial/\partial y)$ is the two-dimensional gradient operator. In the above system, the first two equations are connected with the conservation of fluid mass and momentum, respectively, and represent a depth-averaged subset that is similar to the common Boussinesq-type equations. The last equation is a Poisson equation that accounts for the three-dimensional dynamics and it is used to derive the dispersive contributions. Here, Υ represents the semi-averaged (i.e. over a portion of the water column) vertical component of the velocity field, $\boldsymbol{M}$ is the generalized mass flux and $\boldsymbol{R}$ contains the vorticity contributions to the Poisson equation. These are given by the following expressions:

$$\Upsilon \,=\, \int_z^{\epsilon\eta} w\, d\zeta\,, \qquad \boldsymbol{M} \,=\, \boldsymbol{Q} \,+\, \mu^2 \int_{-h}^{\epsilon\eta} \nabla \Upsilon \mathrm{d}z\,, \tag{3}$$

$$\boldsymbol{R} \,=\, (\, I[\,\mathcal{R}_1\,]\,,\, I[\,\mathcal{R}_2\,]\,)\,, \quad \mathcal{R}_1 \,=\, -\int_z^{\epsilon\eta} \omega_2\, \mathrm{d}\zeta\,, \quad \mathcal{R}_2 = \int_z^{\epsilon\eta} \omega_1\, \mathrm{d}\zeta\,, \tag{4}$$

and the operator $I[\,]$ used in equation (4) is defined as:

$$I[f] \,=\, f \,-\, \frac{1}{d} \int_{-h}^{\epsilon\eta} f\, \mathrm{d}\zeta\,, \tag{5}$$

where f is a generic scalar or vector function. The variable w denotes the vertical component of the velocity field and $\boldsymbol{\omega} = (\omega_1, \omega_2, \omega_3)$ is the vorticity. As usual, $\boldsymbol{Q} = (U_1 d, U_2 d)$ indicates the mass flux and $\boldsymbol{U} = (U_1, U_2)$ is the depth-averaged velocity in the horizontal plane. All

terms associated with linear dispersion are included inside the generalized mass flux $\boldsymbol{M}$ through the integral of $\nabla\Upsilon$. Incidentally, we underline that this structure of the momentum equations is somehow similar to that shown in many Boussinesq-type models (see, for example, Wei et al.[12], Shi et al.[13]) and avoids the presence of time derivatives in the flux tensor $\mathbb{F}$. The latter one includes the remaining dispersive contributions and the classic shallow-water terms:

$$\mathbb{F} = \left(\frac{d^2}{2\,\epsilon} \,+\, \epsilon\,\mu^2 D_{isp} \,+\, \mu^2\, D^T_{isp} \right) \mathbb{1} + \epsilon \left(d\,\boldsymbol{U}\otimes\boldsymbol{U} + \int_{-h}^{\epsilon\eta} (\delta\boldsymbol{u}\otimes\delta\boldsymbol{u})\,\mathrm{d}z \right) + \mu^2\,\mathbb{H}^T\,, \quad (6)$$

where $\otimes$ indicates the dyadic product, the superscript 'T' denotes the turbulent terms and $\delta\boldsymbol{u}$ represents the deviation of the horizontal velocity field, namely $\boldsymbol{u} = (u_1, u_2)$, with respect to the depth-averaged field $\boldsymbol{U}$. These are linked through the following relations:

$$\boldsymbol{u} \,=\, \boldsymbol{U} \,+\, \delta\boldsymbol{u}\,, \qquad \delta\boldsymbol{u} \,=\, -\,\mu^2\, I\,[\,\nabla\Upsilon\,] \,+\, \boldsymbol{R}\,. \quad (7)$$

The term D_{isp} contains the non-linear dispersive contributions coming from the integral of the dynamic pressure:

$$D_{isp} \,=\, \nabla\cdot\left(\int_{-h}^{\epsilon\eta}\int_{z}^{\epsilon\eta} w\,\boldsymbol{u}\,\mathrm{d}\zeta \right) \,-\, \int_{-h}^{\epsilon\eta} w\,(w + \boldsymbol{u}\cdot\nabla h)\,\mathrm{d}z \quad (8)$$

while D^T_{isp} accounts for the corresponding turbulent stresses. Denoting by $(\hat{u}, \hat{v}, \hat{w})$ the turbulent velocity components and by $\langle\cdot\rangle$ the Reynolds average, it reads:

$$\begin{aligned} D^T_{isp} \,=\, & \left(\int_{-h}^{\epsilon\eta} \mathrm{d}z \int_{z}^{\epsilon\eta} \langle \hat{u}\hat{w} \rangle \;\mathrm{d}\zeta \right)_x \,+\, \left(\int_{-h}^{\epsilon\eta} \mathrm{d}z \int_{z}^{\epsilon\eta} \langle \hat{v}\hat{w} \rangle \;\mathrm{d}\zeta \right)_y \,-\, d\,\tau_F^{(z)} \,+ \\ & - \int_{-h}^{\epsilon\eta} \big(\langle \hat{u}\hat{w} \rangle\, h_x + \langle \hat{v}\hat{w} \rangle\, h_y + \langle \hat{w}^2 \rangle \big)\,\mathrm{d}z\,. \end{aligned} \quad (9)$$

where $\tau_F^{(z)}$ indicates the turbulent stresses at the free surface:

$$\tau_F^{(z)} = \langle \hat{u}\hat{w} \rangle \,\big|_{\epsilon\eta}\, \epsilon\,\eta_x \,+\, \langle \hat{v}\hat{w} \rangle \,\big|_{\epsilon\eta}\, \epsilon\,\eta_y \,-\, \langle \hat{w}^2 \rangle \,\big|_{\epsilon\eta}\,. \quad (10)$$

Finally, $\mathbb{H}^T$ contains the remaining turbulent contributions to the momentum flux:

$$\mathbb{H}^T \,=\, \begin{pmatrix} \displaystyle\int_{-h}^{\epsilon\eta} \langle \hat{u}^2 \rangle\,\mathrm{d}z & \displaystyle\int_{-h}^{\epsilon\eta} \langle \hat{u}\hat{v} \rangle\,\mathrm{d}z \\ \\ \displaystyle\int_{-h}^{\epsilon\eta} \langle \hat{u}\hat{v} \rangle\,\mathrm{d}z & \displaystyle\int_{-h}^{\epsilon\eta} \langle \hat{v}^2 \rangle\,\mathrm{d}z \end{pmatrix} \quad (11)$$

The source term in the momentum equation includes the bottom friction $\boldsymbol{\tau}_b$, the dynamic pressure component at the seabed p_b and the related turbulent contribution p_b^T. For what concerns $\boldsymbol{\tau}_b$, this can be modelled by using the standard formulations available in the literature, i.e. simple quadratic drag laws. This makes the bed shear stress proportional to the square of the depth-averaged velocity through a dimensionless friction coefficient, which, in principle, depends on both the local water depth and the bed roughness (i.e. through a dimensionless roughness). Numerous studies, e.g. Puleo and Holland [14], demonstrated that 0.01 can be taken as "an order of magnitude value" for such a coefficient in the case of nearshore flows on medium sand. Conversely, p_b and p_b^T are given below:

$$p_b \,=\, \nabla \cdot \left(\int_{-h}^{\epsilon\eta} w\, \boldsymbol{u}\, \mathrm{d}\zeta \right) \tag{12}$$

$$p_b^T \,=\, \left(\int_{-h}^{\epsilon\eta} \langle \hat{u}\hat{w} \rangle \, \mathrm{d}\zeta \right)_x + \left(\int_{-h}^{\epsilon\eta} \langle \hat{v}\hat{w} \rangle \, \mathrm{d}\zeta \right)_y \,-\, \tau_F^{(z)} \,-\, \tau_B^{(z)} \,, \tag{13}$$

where $\tau_B^{(z)}$ indicates the turbulent stresses at the seabed:

$$\tau_B^{(z)} \,=\, \langle \hat{u}\hat{w} \rangle \big|_{-h} h_x \,+\, \langle \hat{v}\hat{w} \rangle \big|_{-h} h_y \,+\, \langle \hat{w}^2 \rangle \big|_{-h} \,. \tag{14}$$

In the modelling of coastal dynamics, under the assumption of short wind fetches or negligible wind forcing, it is a common practice to assume $\tau_F^{(z)} = 0$.

A. The Poisson equation

In the original work of Antuono and Brocchini [1], two different Poisson equations were derived for the dynamics in the vertical direction. One was expressed in the variable Υ (like in the present case), the other was written in the variable w (the vertical velocity component) and was derived by differentiating the former one by z. In Antuono and Brocchini [1], the equation for w was preferred since the boundary conditions at the bottom and at the free surface were directly available from the kinematic conditions, namely:

$$w|_{\epsilon\eta} \,=\, \eta_t \,+\, \epsilon\, \boldsymbol{u}|_{\epsilon\eta} \cdot \nabla\eta \,, \qquad w|_{-h} \,=\, -\,\frac{h_t}{\epsilon} \,-\, \boldsymbol{u}|_{-h} \cdot \nabla h \,. \tag{15}$$

In this case the main drawback was the evaluation of the velocity components $\boldsymbol{u}|_{\epsilon\eta}$ and $\boldsymbol{u}|_{-h}$, since these depend on the solution itself and, consequently, proper approximations were needed to close the scheme. Apart from this, the numerical implementation of

the Poisson equation for w proved to be a challenging problem. First, the use of the Dirichlet assignment at the free surface proved to be a source of numerical instability for the scheme. During our analysis, we tried different time integrators (classic second-order Muscle-Hancock algorithm, fourth-order Runge-Kutta and fourth-order Adams-Bashforth-Moulton schemes), we implemented both second- and fourth-order reconstruction on the depth-averaged variables, we rearranged the flux tensor, in order to eliminate the presence of time derivatives (see the original model of Antuono and Brocchini [1]), we solved the Poisson equation on a staggered grid with respect to that of the depth-averaged subset, no one of these approaches led to a stable numerical scheme. We argued that the main cause for instability is in the conflict between the Dirichlet assignment at the free-surface and the continuity equation of the depth-averaged subset, these sharing the same nature. In fact, the time derivative in the continuity equation directly comes from the kinematic condition at the free surface. In confirmation of this, a significant improvement was achieved by replacing the Dirichlet assignment at the free surface with a Neumann condition (the expression of the Neumann condition for w is not reported here). This allowed for the construction of a stable scheme which proved however to be inaccurate for highly non-linear waves (e.g. solitary waves with $\epsilon \geq 0.4$), showing the occurrence of spurious high-frequency oscillations during the early stages of the evolution and of a large non-physical dissipation for longer times.

These problems led us to reconsider the Poisson equation for Υ. The key point of this second approach relies on the definition of the generalized flux $\boldsymbol{M}$ and on the observation that the forcing term of the Poisson equation actually depends on it. The second fundamental point is the structure of the boundary conditions for Υ (the details of computation are given in Appendix B). These are a Dirichlet condition along the free-surface and a Neumann condition along the seabed:

$$\Upsilon|_{\epsilon\eta} = 0\,, \qquad \left.\frac{\partial \Upsilon}{\partial n}\right|_{-h} = -\left[\frac{h_t}{\epsilon} + \left(\frac{\boldsymbol{M}}{d} + \boldsymbol{R}\big|_{-h}\right)\cdot\nabla h\right] \Big/ \sqrt{1+\mu^2\|\nabla h\|^2}\,, \quad (16)$$

where $\boldsymbol{n}$ is the outer unit vector to the seabed. Differently from the Poisson equation for w, the above boundary conditions lead to a closed formulation, since both η and $\boldsymbol{M}$ are obtained by the time-integration of the depth-averaged equations of system (2). A further strong point of this approach is that, differently from w, the variable Υ represents itself a depth semi-averaged (i.e. over a portion of the water column) quantity and, therefore, it

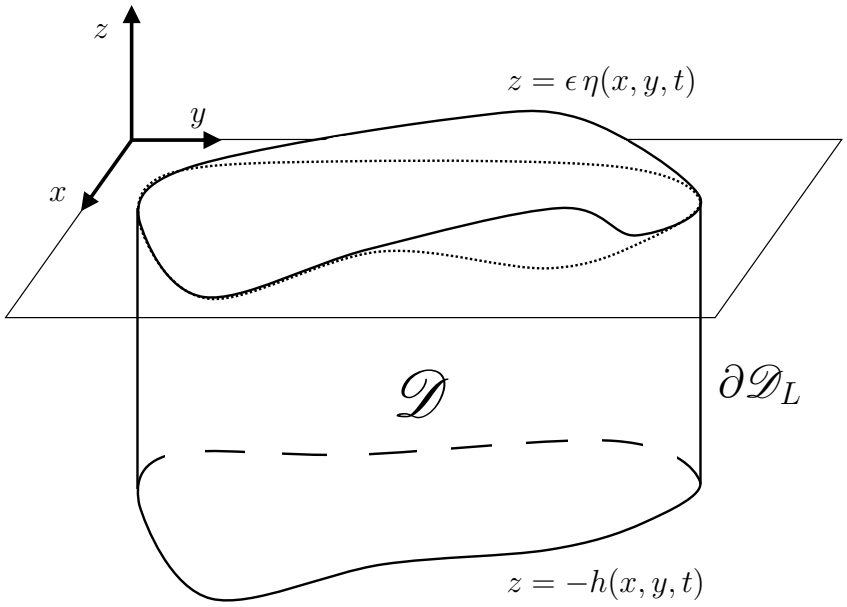

FIG. 2. Sketch of the fluid domain $\mathscr{D}$. The horizontal plane denotes the still water level, the dotted lines indicate the intersection between $\mathscr{D}$ and the still water level and $\partial\mathscr{D}_L$ is the lateral boundary.

is somehow "closer" to the set of depth-averaged equations [namely, the first two equations of system (2)]. Considering a fluid domain $\mathscr{D}$ like that depicted in figure 2, the Poisson equation for Υ along with the corresponding boundary conditions reads:

$$\begin{cases} \mu^2\,\Upsilon_{xx} \,+\, \mu^2\,\Upsilon_{yy} \,+\, \Upsilon_{zz} \,=\, \nabla\cdot\left(\dfrac{\boldsymbol{M}}{d}+\boldsymbol{R}\right), \\[2ex] \Upsilon|_{\epsilon\eta} \,=\, 0\,, \\[2ex] \left.\dfrac{\partial\Upsilon}{\partial n}\right|_{-h} = -\left[\dfrac{h_t}{\epsilon} \,+\, \left(\dfrac{\boldsymbol{M}}{d} \,+\, \boldsymbol{R}\big|_{-h}\right)\cdot\nabla h\right]\Big/\sqrt{1+\mu^2\|\nabla h\|^2}\,, \\[2ex] \mu^2\,\Upsilon\big|_{\mathscr{D}_L} \,=\, c_D\,, \qquad \text{or} \qquad \mu^2\left.\dfrac{\partial\Upsilon}{\partial n}\right|_{\mathscr{D}_L} \,=\, c_N\,, \end{cases} \tag{17}$$

Two alternative boundary conditions may be considered along $\mathscr{D}_L$. The Dirichlet assignment is obtained through the definition of Υ in (3) and the knowledge of w at $\mathscr{D}_L$. Conversely, using the definition of $\boldsymbol{M}$ in (3) and that of $\delta\boldsymbol{u}$ in (7), it is simple to prove that the Neumann condition is related to the following quantities along $\mathscr{D}_L$:

$$I[c_N] \,=\, (\,\boldsymbol{R} \,-\, \delta\boldsymbol{u}\,)\,\big|_{\mathscr{D}_L}\cdot\boldsymbol{n} \qquad \int_{-h}^{\epsilon\eta} c_N\,\mathrm{d}z \,=\, (\,\boldsymbol{M} \,-\, \boldsymbol{Q}\,)\,\big|_{\mathscr{D}_L}\cdot\boldsymbol{n}\,.$$

In practice, this condition takes into account the deviations of the local velocity and of the generalized momentum with respect to the usual depth-averaged quantities, namely $\boldsymbol{U}$ and $\boldsymbol{Q}$. In the following sections we give the details of the numerical implementation of the system (2) and show the results of some relevant test cases.

III. NUMERICAL IMPLEMENTATION

A. The depth-averaged subset

Let us consider the subset of depth-averaged equations in (2) and recast it in the following simple structure:

$$\boldsymbol{\Psi}_t \,=\, \boldsymbol{E} \tag{18}$$

where $\boldsymbol{\Psi} = (d, M_1, M_2)$ and $\boldsymbol{E}$ indicates the corresponding flux components. Specifically, we assume that at any given time step, say $t^{(n)}$, all the variables derived from the solution for Υ are known. Following Wei et al.[12], the system in (18) is integrated in time by using a fourth-order Adams-Bashforth-Moulton predictor/corrector scheme (ABM hereinafter). In the present case, its main advantage lays in the minimization of the number of times that the 3D solution has to be computed in comparison to the order of accuracy of the scheme.

The Adams-Bashforth predictor step is given by:

$$\boldsymbol{\Psi}_*^{(n+1)} \,=\, \boldsymbol{\Psi}^{(n)} \,+\, c_n\, \boldsymbol{E}^{(n)} \,+\, c_{n-1}\, \boldsymbol{E}^{(n-1)} \,+\, c_{n-2}\, \boldsymbol{E}^{(n-2)}\,, \tag{19}$$

where c_n, c_{n-1}, c_{n-2} are known coefficients and the fluxes $E^{(n)}, E^{(n-1)}, E^{(n-2)}$ have been computed at the time steps t^n, t^{n-1}, t^{n-2}. If the time step is constant, say Δt, the scheme described in (19) is accurate to the third order in time and the coefficients are:

$$c_n \,=\, \frac{23}{12}\,\Delta t\,, \qquad c_{n-1} \,=\, -\frac{4}{3}\,\Delta t\,, \qquad c_{n-2} \,=\, \frac{5}{12}\,\Delta t\,.$$

The predicted value $\boldsymbol{\Psi}_*^{(n+1)}$ allows one to compute the boundary data of the Poisson equation for Υ. Its solution, namely $\Upsilon_*^{(n+1)}$, is then used to evaluate $\delta\boldsymbol{u}, D_{isp}$, etc. and, consequently, the predicted flux $\boldsymbol{E}_*^{(n+1)}$. Finally, this is included in the corrector step (i.e. Adams-Moulton step) as follows:

$$\boldsymbol{\Psi}^{(n+1)} \,=\, \boldsymbol{\Psi}^{(n)} \,+\, \hat{c}_{n+1}\, \boldsymbol{E}_*^{(n+1)} \,+\, \hat{c}_n\, \boldsymbol{E}^{(n)} \,+\, \hat{c}_{n-1}\, \boldsymbol{E}^{(n-1)} \,+\, \hat{c}_{n-2}\, \boldsymbol{E}^{(n-2)}\,. \tag{20}$$

If the time step is constant, the scheme described in (20) is accurate to the fourth order in time and the coefficients are:

$$\hat{c}_{n+1} = \frac{9}{24}\Delta t\,, \quad \hat{c}_n = \frac{19}{24}\Delta t\,, \quad \hat{c}_{n-1} = -\frac{5}{24}\Delta t\,, \quad \hat{c}_{n-2} = \frac{1}{24}\Delta t\,.$$

Since the fluxes $\boldsymbol{E}^{(n-1)}$, $\boldsymbol{E}^{(n-2)}$ are both available for $n > 2$, a fourth-order Runge-Kutta scheme has been used for $n \leq 2$. The time step is computed by using the solution at time $t^{(n)}$. For a Cartesian grid with spacing $(\Delta x_i, \Delta y_i)$, it reads:

$$\Delta t^{n+1} = t^{n+1} - t^n = C\,\min\left[\min_i\left(\frac{\Delta x_i}{\left|U_{1,i}^{(n)}\right| + \sqrt{g\,d_i^{(n)}}}\right), \min_i\left(\frac{\Delta y_i}{\left|U_{2,i}^{(n)}\right| + \sqrt{g\,d_i^{(n)}}}\right)\right],$$

where C is the Courant-Friedrichs-Lewy number, here set equal to 0.4.

The last part is dedicated to the computation of the numerical flux $\boldsymbol{E}$ which, for the depth-averaged subset, may be decomposed as follows:

$$\boldsymbol{E} = -\nabla\cdot\mathbb{G} + \boldsymbol{S}\,, \tag{21}$$

where $\mathbb{G}$ is the flux tensor and $\boldsymbol{S}$ is the forcing term. The term $\nabla\cdot\mathbb{G}$ is written in a weak formulation by integration over the cell volume and the corresponding fluxes across the cell sides, namely $\mathbb{G}\cdot\boldsymbol{n}$, are evaluated through the MUSCLE-Hancock scheme with the HLL approximate Riemann solver described in Toro[15,16], initially conceived for hyperbolic equations. This scheme appears to be the most suited for the problem at hand since the subset of depth-averaged equations is written in a conservative fashion. In any case, its implementation for dispersive equations is quite a common practise in the literature on Boussinesq-type equations (see, for example, Shi et al.[13], Kim et al.[17]). Very briefly, the adopted MUSCLE-Hancock scheme consists in a first step in which the variables to be used for the flux evaluation are reconstructed at the cell sides. Specifically, for the depth-averaged variables (e.g. η, $\boldsymbol{U}$) we implemented the fourth-order data reconstruction described in Yamamoto and Daiguji[18] with parameters $b_1 = 2$ and $b = 3$ as suggested in Kim et al.[17]. Conversely, we used a second-order reconstruction with the MINMOD limiter for the quantities deriving from the solution for Υ (e.g. D_{isp}, p_b, etc.). The approach described above is somehow similar to that used by Wei et al.[12] where fourth-order accuracy was achieved for first-order derivatives while second-order accuracy for the dispersive terms. To make the scheme well-balanced, we implemented the surface gradient of Zhou et al.[19],

which prescribes the reconstruction of the free-surface signal η rather than the total water depth d. Similarly, to avoid the occurrence of spurious oscillations caused by the data reconstruction in very shallow depths, the reconstruction of $\boldsymbol{U}$ is preferred to that of the mass flux $\boldsymbol{Q}$. This does not alter the correctness of the conservation relations for the depth-averaged subset, since the approximate Riemann solver is applied to the correct conservative equations (i.e. the equations expressed in terms of the conservative variables $d, \boldsymbol{Q}$). Finally, the reconstructed data are used in the HLL solver to compute the fluxes at the cell sides and to find the values of d and $\boldsymbol{M}$ at the new time instant. Specifically, the updated value of the water depth (obtained from the integration of the continuity equation) is, first, used to update the hydrostatic contribution in the source term $\boldsymbol{S}$ (namely, $d\,\nabla h$). Then, the updated value of the generalized mass flux $\boldsymbol{M}$ is computed.

B. The solution for Υ

After the corrector step of the ABM scheme is completed, the updated quantities (d, M_1, M_2) are available at the new time $t^{(n+1)}$. These are used to evaluate the boundary conditions in equation (17) and, then, to obtain $\Upsilon_*^{(n+1)}$ through the solution of the Poisson equation. This is discretized by second-order finite differences over a uniform Cartesian grid and, then, solved through the GMRES iterative method (namely, Generalized Minimal RESidual Method). Specifically, we used the MUltifrontal Massively Parallel Solver (MUMPS) described in Amestoy and Duff[20], Amestoy et al.[21] and available at $http://mumps.enseeiht.fr/$.

Neumann conditions have been enforced by using a diffuse boundary approach, as described in Li X. et al.[22]. In brief, the Poisson equation in (17) is solved over a domain $\mathscr{D}_\delta$ that is obtained by diffusing the original domain $\mathscr{D}$ in the normal outer direction over a reference smoothing length δ. Then, the equation is modified as follows:

$$\hat{\nabla} \cdot \Big(H\, \hat{\nabla} \Upsilon \Big) \,-\, H\, f \,+\, c_N \,\|\hat{\nabla} H\| \,=\, 0 \tag{22}$$

where $\hat{\nabla} = (\mu\, \partial/\partial x,\, \mu\, \partial/\partial y,\, \partial/\partial z)$, f is the original forcing term in the governing equation for Υ and the function H represents a step-like function that is null outside $\mathscr{D}_\delta$ and grows smoothly to 1 inside $\mathscr{D}_\delta$ over the length δ. By construction, the gradient of H is normal to the physical domain boundary, $\partial\mathscr{D}$, and tends to a Dirac function along $\partial\mathscr{D}$ as δ goes

to zero. The datum c_N indicates the "diffuse" Neumann condition on $\mathscr{D}$ and it is obtained by extending the original Neumann datum uniformly in the normal direction given by $\hat{\nabla} H$. Thanks to this procedure, the assignment of the Neumann condition is obtained implicitly in the solution of the linear equation (22). A further important point is that the function H, being related to the bottom bathymetry, does not depend on time and, therefore, is just evaluated at the initial time. Finally, Dirichlet conditions are assigned exactly at the free surface where it intersects the Cartesian grid. This is done by locally discretizing the Poisson equation through finite-difference operators with variable grid spacing and imposing $\Upsilon = 0$ at the intersection points. This procedure is straightforward, since the free-surface elevation is known at each time step from the solution of the depth-averaged subset.

C. Evaluation of the source and flux terms

Once the solution for Υ is computed, we need to evaluate the remaining variables in the source and flux terms. First, we obtain the mass flux $\boldsymbol{Q}$ from the solution of $\boldsymbol{M}$ at $t^{(n+1)}$ through the second equation in (3). Actually, we use the following equivalent expression (we recall that Υ is null along the free surface):

$$\boldsymbol{M} \,=\, \boldsymbol{Q} \,+\, \mu^2 \nabla \left(\int_{-h}^{\epsilon\eta} \Upsilon \mathrm{d}z \right) \,-\, \mu^2 \, \Upsilon\big|_{-h} \nabla h \,, \tag{23}$$

since this ensures the conservation of the mass flux when the bottom bathymetry is planar. The gradient of the integral is here computed through a central fourth-order finite difference. Conversely, a central second-order finite difference is used for the spatial derivatives in the remaining terms (e.g. D_{isp}, p_b, etc.). Finally, the integration over the fluid depth has been made through the Simpson's rule.

D. Flow chart

The numerical scheme is summarized in the following diagram:

•: INITIALIZATION

1. Assign the initial/boundary data for the depth-averaged equations (e.g. variables $\eta, \boldsymbol{U}$) and initialize $\boldsymbol{M} = \boldsymbol{Q}$;

2. evaluate the boundary conditions for the Poisson equation;

3. solve the Poisson equation for Υ;

4. compute the dispersive terms from the Poisson solution (that is $\delta\boldsymbol{u}$, $\boldsymbol{M}$, ...);

5. iterate points 2), 3) and 4) until convergence;

•: EVOLUTION

•: Predictor step

- **∘:** read the boundary data for the depth-averaged equations at time $t^{(n)}$;
- **∘:** evaluate the fluxes of the depth-averaged equations at time $t^{(n)}$ through the HLL Riemann solver;
- **∘:** compute the predicted momentum $\boldsymbol{M}_*^{(n+1)}$ and the predicted wave elevation $\eta_*^{(n+1)}$ through the third-order Adams-Bashforth predictor step;
- **∘:** evaluate the boundary conditions for the Poisson equation at time $t^{(n+1)}$;
- **∘:** solve the Poisson equation for $\Upsilon_*^{(n+1)}$;
- **∘:** compute the dispersive terms from the Poisson solution. Compute the predicted mass flux $\boldsymbol{Q}_*^{(n+1)}$ through equation (23);

•: Corrector step

- **∘:** read boundary data for the depth-averaged equations at time $t^{(n+1)}$;
- **∘:** evaluate the fluxes of the depth-averaged equations at time $t^{(n+1)}$ through the HLL Riemann solver;
- **∘:** compute the momentum $\boldsymbol{M}^{(n+1)}$ and the wave elevation $\eta^{(n+1)}$ through the fourth-order Adams-Moulton corrector step;
- **∘:** evaluate the boundary conditions for the Poisson equation;
- **∘:** solve the Poisson equation for $\Upsilon^{(n+1)}$;
- **∘:** compute the dispersive terms from the Poisson solution. Compute the corrected mass flux $\boldsymbol{Q}^{(n+1)}$ through equation (23);

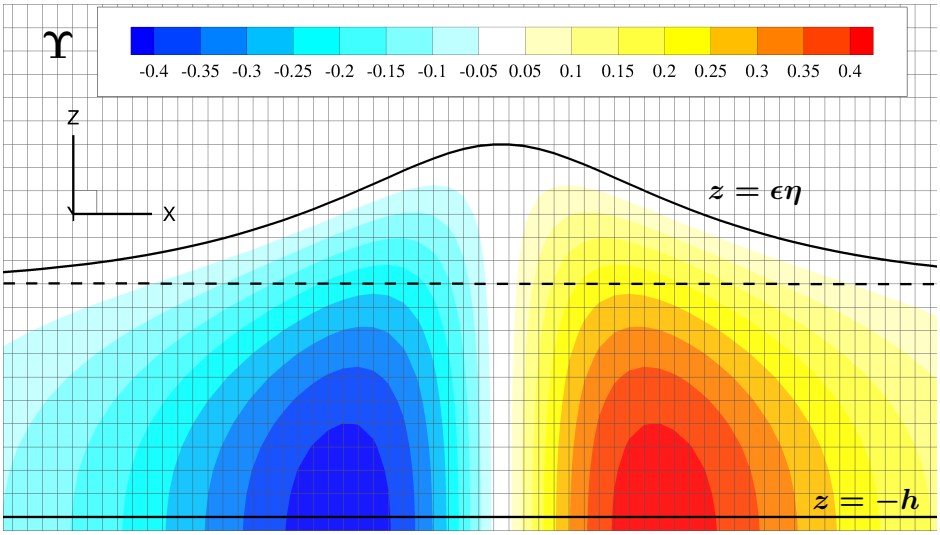

FIG. 3. Initial solution for Υ for the case of a solitary wave with $\epsilon = 0.6$. The thick solid lines indicate the free-surface elevation and the seabed while the dashed line denotes the still water level.

IV. APPLICATIONS

In the present section we propose some selected two-dimensional test cases to show the model features. Since this is meant to be a preliminary work, we neglect all the turbulence and vorticity dynamics terms and leave the analysis of the complete model for future studies. The scheme is initialized by assigning the depth-averaged variables (namely, d, $\boldsymbol{U}$) while the generalized momentum $\boldsymbol{M}$ is obtained through an iterative procedure. Specifically, at the first iteration $\boldsymbol{M}$ is approximated as $\boldsymbol{Q} = \boldsymbol{U}d$ and it is used to compute the forcing term and the boundary conditions of the Poisson equation (17). This provides a first approximate solution for Υ, which is used to obtain a new value of $\boldsymbol{M}$ through the definition in equation (23). Then, the procedure is repeated until the relative error between two subsequent iterations in the L^∞-norm is below 0.01, that is:

$$\varepsilon_r = \frac{\| \Upsilon^{(k+1)} - \Upsilon^{(k)} \|_\infty}{\| \Upsilon^{(k+1)} \|_\infty} < 0.01\,. \tag{24}$$

Generally, few iterations are enough to ensure an accurate initial value for $\boldsymbol{M}$.

A. The solitary wave

The first example is the 2D propagation of a solitary wave over a flat bottom (all the lengths have been made dimensionless by the still water depth h_0^*). The analytical solution

predicts that the solitary wave translates with a permanent profile at a constant velocity F_r (Froude number). The numerical scheme is initialized through the ninth-order analytical solution described in Fenton [23] over a fluid domain $\mathscr{D} = [0, 40] \times [-1.45, 1.45]$ with periodic boundary conditions along the x-direction. The still water elevation and the seabed are at $z = 0$ and $z = -1$, respectively, while the crest of the solitary wave is placed at $x = 20$. The domain is discretized through a uniform Cartesian grid with spatial steps $\Delta x = \Delta z = 0.1$ and three different wave amplitudes are analysed, namely $\epsilon = 0.2, 0.4, 0.6$, ranging from mild to highly non-linear waves. The Froude numbers associated with the above parameters are $F_r = 1.094, 1.178, 1.250$, respectively. Incidentally, we recall that the parameter μ is implicit in the solution of the solitary wave and, therefore, it is not specified. The initial configuration is drawn in figure 3 for $\epsilon = 0.6$ along with the solution for Υ. The vertical discretization in use is very coarse in comparison with the wave elevation. The ability of modelling such a steep wave using a coarse resolution is one of the main advantages of the proposed scheme and relies on the fact that, at each time instant, the free-surface is known after the integration of the depth-averaged subset.

The solutions for the free surface η and the generalized momentum M (x-component) are displayed in figures 4 ($\epsilon = 0.2$) and 5 ($\epsilon = 0.6$) after the solitary wave has travelled for ten times over the periodic domain. In the mildly non-linear case, both signals (i.e., the analytical solution for η and the converged iterated datum for M) are practically superposed to the initial data. On the contrary, a small damping is observed near the crest for $\epsilon = 0.6$, that is for the strongly non-linear case. This might be expected because of the large steepness of this solitary wave but, in any case, the results are still satisfactory. With respect to this, we observe that the same test case has been described in Wei et al. [12]. In that work, the authors needed to initialize the solitary wave by trial and error since the wave tended to resettle to different wave heights during the initial transient. Further, spurious oscillations were observed and a long evolution was necessary to damp them out and obtain a clear solitary wave profile. In the present case, no spurious oscillations are observed and, apart from the numerical wave damping, the initial wave profile is conserved during the whole evolution with very limited dispersive errors.

Table I summarizes the results for the different values of ϵ. Specifically, we consider the absolute relative error $\mathcal{E}_r$ for the free-surface maximum elevation η_{max}, the maximum value of the generalized momentum M_{max} and the Froude number F_r after ten periods of

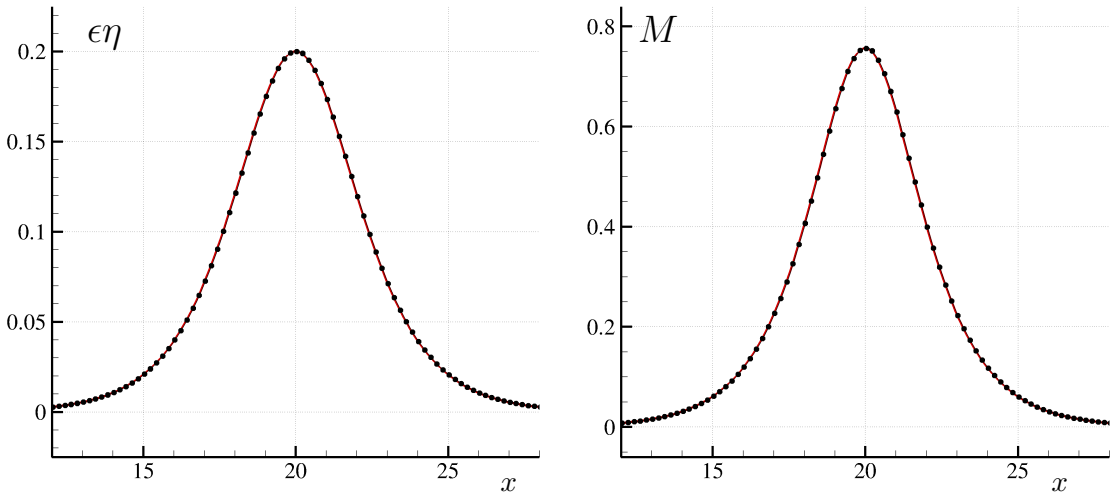

FIG. 4. The solitary wave solution with $\epsilon = 0.2$. Left panel: the free-surface elevation. Right panel: the generalized momentum. The thick solid lines indicate the initial solution while the dots denote the solution after the solitary wave has travelled for ten times over the periodic domain.

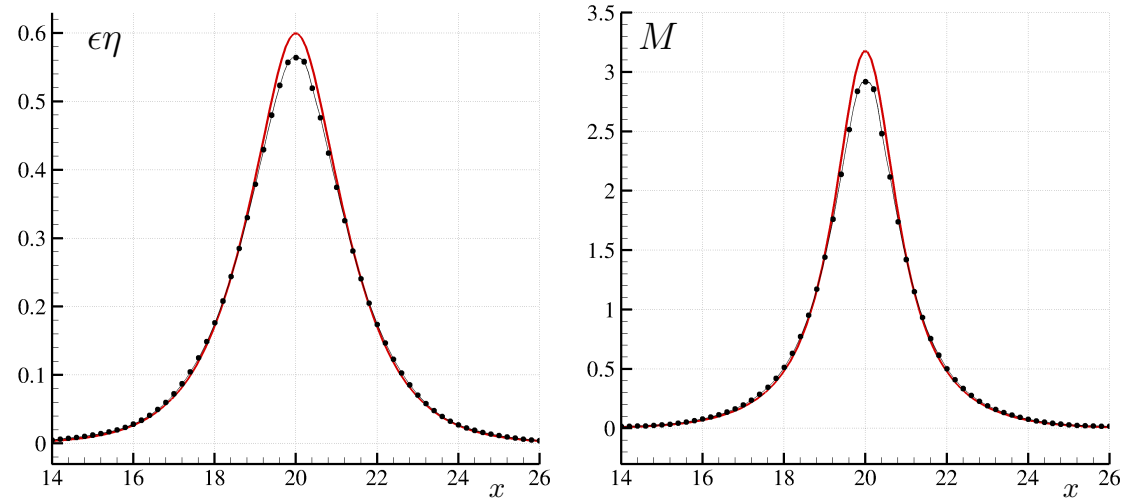

FIG. 5. The solitary wave solution with $\epsilon = 0.6$. Left panel: the free-surface elevation. Right panel: the generalized momentum. The thick solid lines indicate the initial solution while the dots denote the solution after the solitary wave has travelled for ten times over the periodic domain.

evolution in the periodic domain. The absolute relative error $\mathcal{E}_r$ of a scalar non-null quantity f is defined as follows:

$$\mathcal{E}_r\left[f\right] = \frac{|\, f_{num} - f_{an}|}{|f_{an}|} \tag{25}$$

where f_{num} is the numerical output and f_{an} is the analytical solution. The Froude number has been obtained by measuring the position of the maximum wave elevation at the end

TABLE I. Solitary wave solution: absolute relative errors for the maximum free-surface elevation η_{max}, the maximum value of the generalized momentum M_{max} and the Froude number F_r for different values of the non-linearity parameter ϵ. The results refer to the numerical solution after ten periods of evolution in the periodic domain.

ϵ	$\mathcal{E}_r\,[\eta_{max}]$	$\mathcal{E}_r\,[M_{max}]$	$\mathcal{E}_r\,[F_r]$
0.2	$4.1 \cdot 10^{-4}$	$9.8 \cdot 10^{-4}$	$8.17 \cdot 10^{-5}$
0.4	$1.0 \cdot 10^{-2}$	$7.7 \cdot 10^{-3}$	$3.38 \cdot 10^{-4}$
0.6	$6.0 \cdot 10^{-2}$	$5.7 \cdot 10^{-2}$	$4.26 \cdot 10^{-3}$

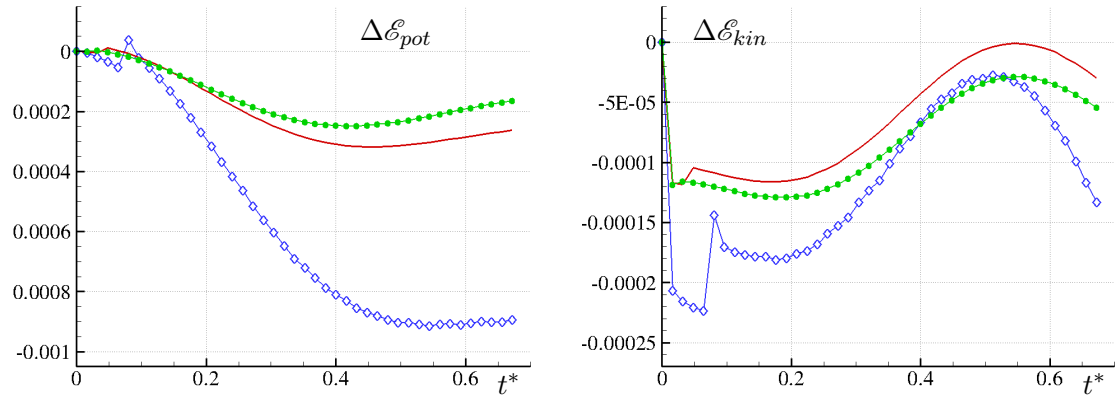

FIG. 6. The solitary wave solution with $\epsilon = 0.4$. Left panel: convergence of the global potential energy, namely $\Delta\mathscr{E}_{pot} = \mathscr{E}_{pot}/\mathscr{E}^0_{pot} - 1$. Right panel: convergence of the global kinetic energy, namely $\Delta\mathscr{E}_{kin} = \mathscr{E}_{kin}/\mathscr{E}^0_{kin} - 1$. The superscript '0' indicates the value at the initial time. In all panels the solid lines indicate the reference solution while the symbols '•' and '◇' denote the finest and the coarsest resolutions, respectively.

of the evolution and comparing it to the analytical prediction. Table I clearly shows that the relative errors maintain very small for $\epsilon = 0.2, 0.4$ while a slight increase is observed for $\epsilon = 0.6$, which represents a very steep wave in practice. In any case, the outputs are satisfactory and confirm the accuracy of the proposed scheme.

As a further confirmation, table II displays the convergence rate of the kinetic and potential energy of the depth-averaged subset, that is

$$\mathscr{E}_{kin} = \int_D \frac{\|\boldsymbol{U}\|^2}{2}\, dV\,, \qquad \mathscr{E}_{pot} = \int_D \frac{\eta^2}{2}\, dV\,. \tag{26}$$

Figure 6 displays the early stages of the evolution of both energy components for the case

TABLE II. Solitary wave solution: the convergence rate for the kinetic and potential energy of the depth-averaged subset during the early stages of the evolution.

	kinetic energy			potential energy		
ϵ	L^1-norm	L^2-norm	L^∞-norm	L^1-norm	L^2-norm	L^∞-norm
0.2	1.46	1.45	1.37	2.26	2.28	2.23
0.4	1.39	1.46	2.05	2.92	2.87	2.69
0.6	3.90	3.83	3.53	3.02	3.09	3.45

with $\epsilon = 0.4$. The convergence rate in the L^p-norm, based on a doubling/halving of both the spatial and time resolution, is defined as follows:

$$r_{2,p} = -\log\left(\frac{\|f_{fine} - f_{medium}\|_p}{\|f_{medium} - f_{coarse}\|_p}\right) / \log(2) \tag{27}$$

where f indicates a generic signal, "fine", "medium" and "coarse" refer to the different resolutions and the function "log" indicates the natural logarithm. The "medium" resolution is that described at the beginning of the present section. Table II shows that the converge rate ranges between 2 and 3 for the potential energy while a larger scattering is observed for the kinetic energy, this going from about 1.4 for $\epsilon = 0.2$ to about 3.7 for $\epsilon = 0.6$. The latter behaviour is caused by the large inaccuracy of the coarse resolution for the solitary wave with $\epsilon = 0.6$. In this case, the convergence of the potential energy provides more reliable results.

1. The solitary wave on a planar beach

In the present section we consider the run-up of a solitary wave on a beach with constant slope. This allows us to check how the proposed scheme accounts for the shoaling effects in shallow-water conditions.

First, we consider the experimental test described in Guibourg[24] and reported in Bonneton et al.[25] where solitary waves of different heights propagate from a constant-depth region towards a beach with slope 1:30. Since the beach geometry is composite, there is no unique scaling factor for the lengths and, consequently, we prefer to deal with dimensional variables, except for the time, which is scaled by $t_0^* = \sqrt{h_0^*/g^*}$. The solitary wave crests are initially located at $x^* = 10m$ over a constant bottom with $h_0^* = 0.25m$ while the sloping

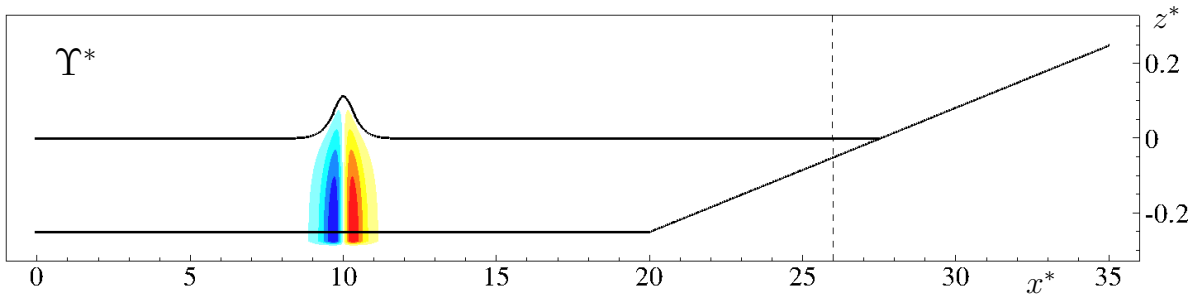

FIG. 7. Shoaling of a solitary wave with initial height $\epsilon = 0.456$ on a 1:30 sloping beach. Sketch of the initial configuration. The dashed line indicates the shoreward limit of the computational domain for the solution of Υ.

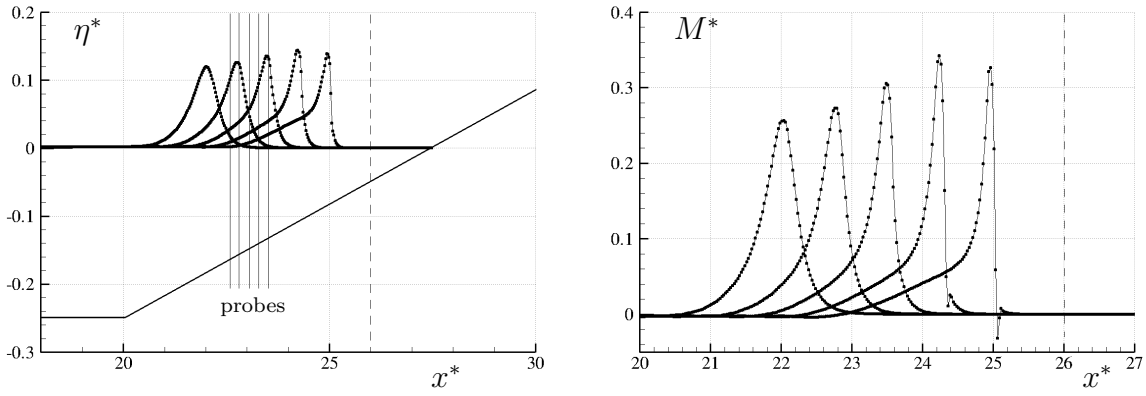

FIG. 8. Shoaling of a solitary wave with initial height $\epsilon = 0.456$ on a 1:30 sloping beach. Snapshots of the evolution at time $t^*\sqrt{g^*/h_0^*} = 40, 42.5, 45, 47.5, 50$ for the wave elevation (left) and the generalized momentum (right). The dashed line indicates the shoreward limit of the computational domain for the solution of Υ. The solid lines on the left panel indicate the positions of the probes.

beach starts at $x^* = 20m$ and the still shoreline is at $x^* = 27.5m$. An open boundary is set at $x^* = 0m$. The spatial discretization is $\Delta x^* = 0.025m$ and $\Delta z^* = 0.0125m$ and two solitary waves are considered with initial height $\epsilon = 0.456$ and $\epsilon = 0.298$, respectively. A sketch of the geometry is depicted in figure 7 for $\epsilon = 0.456$ along with the initial solution for Υ. We underline that the computational domain for Υ is cut when there are less than three computational nodes in the vertical direction. In the remaining part of the domain, Υ is set to zero consistently with the boundary condition at the free surface and the depth semi-averaged system reduce to the Nonlinear Shallow Water Equations. The "cut" is represented in figures 7 and 8 by a vertical dashed line. Along it, a null Dirichlet boundary condition is

TABLE III. Shoaling of a solitary wave over a 1:30 sloping beach: positions of the wave probes.

ϵ	x_1^*	x_2^*	x_3^*	x_4^*	x_5^*
0.456	22.590	22.805	23.060	23.280	23.520
0.289	23.520	23.735	23.990	24.210	24.448
0.100	26.500	26.750	27.000	27.250	27.500

imposed to solve the Poisson equation for Υ.

Free-surface displacements are measured at various locations (see Table III), using numerical wave probes located seaward of the breaking point. A sketch of the probe positions is displayed in figure 8 for $\epsilon = 0.456$, along with the numerical solutions for the free-surface elevation (left) and the generalized momentum (right) at different time instants. Because of the large wave steepness (the wave is on the verge of breaking), small oscillations occur at the toe of the momentum signals for $t^*\sqrt{g^*/h_0^*} = 47.5, 50$ (right panel of figure 8). Apart from this, the numerical outputs are quite regular and predict the shoaling phenomenon during the wave run-up. Quantitative comparisons between the numerical solutions (solid lines) and the experiments (dot-solid lines, Bonneton et al. [25]) are shown in figures 9 and 10 for $\epsilon = 0.456$ and $\epsilon = 0.298$, respectively. In both cases, the overall match is good, both in terms of maximum wave height and shape of the signals. Incidentally, we observe that tail of the solitary wave appears slightly longer than the numerical one. This phenomenon may be due to the difficulties related to the generation of the solitary wave during the experiments, as already pointed out in Bonneton et al. [25].

Since both solitary waves described above break during the run-up stage and no model for wave-breaking is here implemented, the long-time evolution is not examined. In any case, a less nonlinear wave (namely, $\epsilon = 0.1$) has been run to give a qualitative description of how the proposed model behaves during the run-up. Figure 11 displays some snapshots of the evolution of the wave elevation and the generalized momentum at different times. The occurrence of some very weak wave breaking is suggested by the presence of sharp and peaked profiles at $t^*\sqrt{g^*/h_0^*} = 66.6$ and by the subsequent wave collapse at the shoreline. A different view is given in figure 12 where the free-surface elevation is recorded at different positions (see Table III). All the probes are inside the region where the model reduces to the Nonlinear Shallow Water Equations and, in particular, probe x_5^* is at the still shoreline

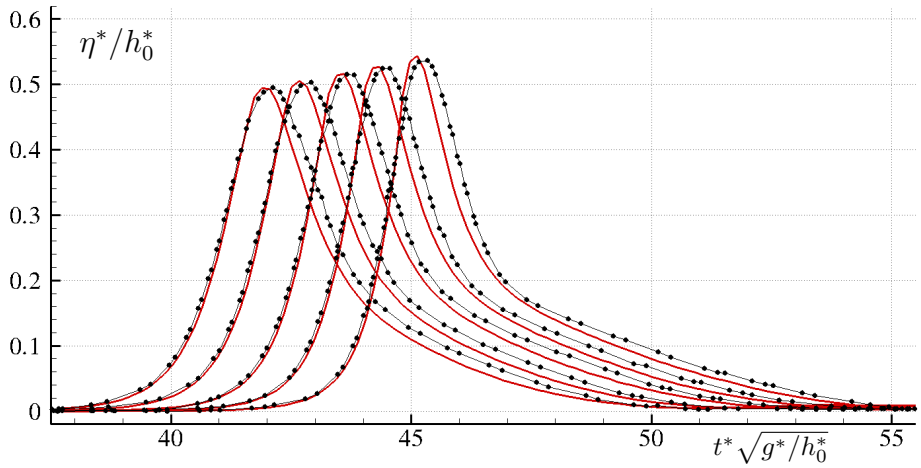

FIG. 9. Shoaling of a solitary wave with initial wave height $\epsilon = 0.456$ on a 1:30 sloping beach. The solid lines indicate the numerical solution while the dot-solid lines the experimental measurements (Bonneton et al.[25]). The probe positions are given in the Table III.

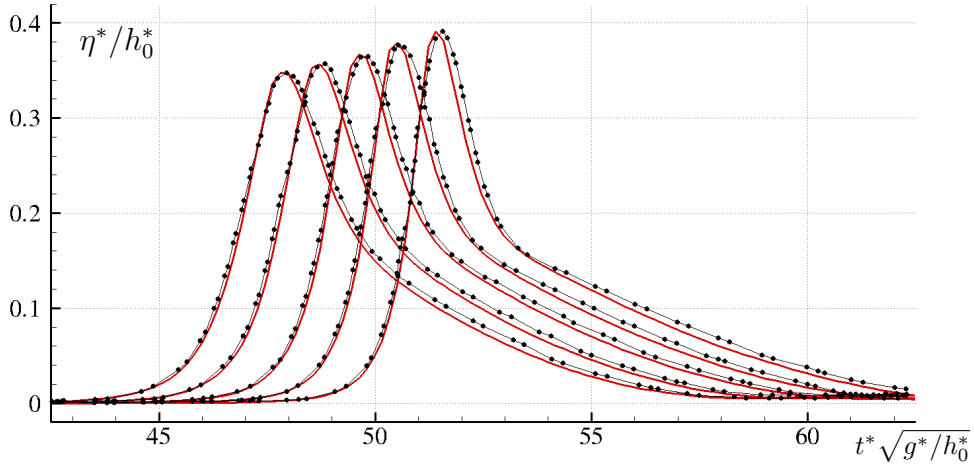

FIG. 10. Shoaling of a solitary wave with initial wave height $\epsilon = 0.298$ on a 1:30 sloping beach. The solid lines indicate the numerical solution while the dot-solid lines the experimental measurements (Bonneton et al.[25]). The probe positions are given in the Table III.

(see Table III). No spurious oscillations are observed when the wave crosses the boundary of the computational domain used for the solution of Υ.

B. Stokes waves

As a final problem we consider the propagation of Stokes waves (i.e. waves of permanent shape that propagate at a constant speed in deep and intermediate waters), this being an

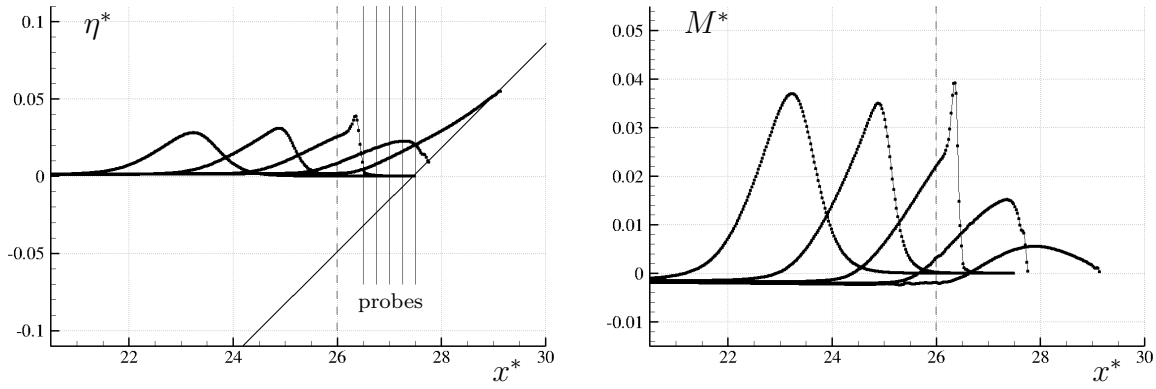

FIG. 11. Shoaling of a solitary wave with initial wave height $\epsilon = 0.1$ on a $1:30$ sloping beach. Snapshots of the evolution at time $t^*\sqrt{g^*/h_0^*} = 51.33, 58.97, 66.60, 74.71, 82.82$ for the wave elevation (left) and the generalized momentum (right). The dashed line indicates the shoreward limit of the computational domain for the solution of Υ. The solid lines on the left plot indicate the positions of the probes.

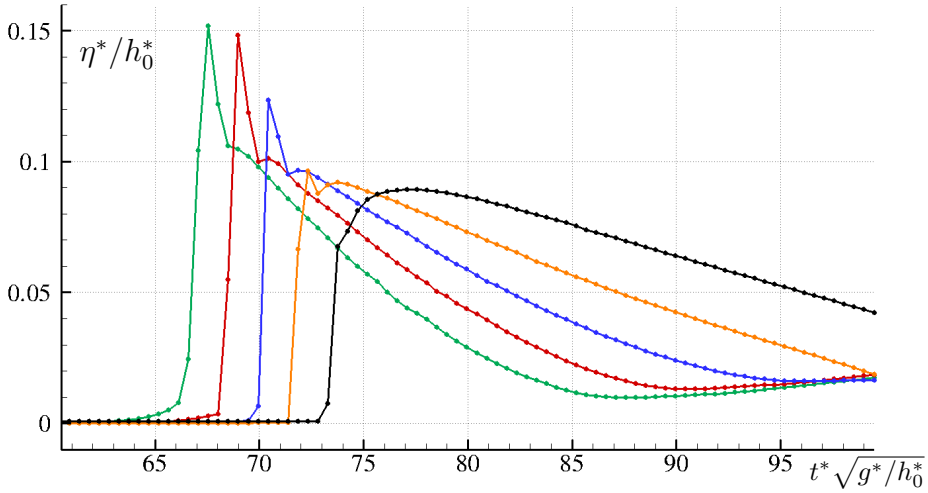

FIG. 12. Shoaling of a solitary wave with initial wave height $\epsilon = 0.1$ on a 1:30 sloping beach. The probe positions are given in Table III.

optimal benchmark for testing the ability of the proposed model in representing the linear dispersion relation. For an exhaustive description of the analytical solution, we refer the interested readers to the book of Méhauté [26].

Three different configurations have been run (see Table IV), these ranging from intermediate waters (e.g., $\mu = \pi/2, 2\pi/3$) to the lower bound of deep waters (i.e., $\mu = \pi$). We first focus on the latter case (namely, case 3 in table IV), since this represents the

TABLE IV. Stokes waves: dispersion parameter (μ), nonlinearity parameter (ϵ) and steepness parameter ($s = \pi H^*/L^* = \epsilon\mu/2$) of the considered test cases. The symbols T^* and c^* denote the dimensional wave period and celerity, respectively.

	μ	ϵ	s	$h_0^*\,(m)$	$L^*\,(m)$	$T^*\,(sec)$	$c^*\,(m/sec)$
case 1	$\pi/2$	0.25	0.196	1	4	1.632	2.451
case 2	$2\pi/3$	0.20	0.209	1	3	1.375	2.182
case 3	π	0.15	0.235	1	2	1.103	1.814

most challenging configuration. In fact, coastal models based on Boussinesq-type equations generally approximate the exact linear dispersion relation and the overall approximation becomes worse and worse as the water deepens. Conversely, as proved in Antuono and Brocchini [1], the present scheme is able to correctly predict both the linear dispersion relation and, at least, the third-order solution for Stokes waves.

We first consider a convergence study during the early stages of the evolution (namely, about three periods of evolution). The reference case is obtained for $L^*/\Delta x^* = 20$, $h_0^*/\Delta z^* = 10$ (uniform Cartesian grid) and the initial solution for Υ is illustrated in the top left panel of figure 13. The convergence analysis focuses on the variation of the potential energy, i.e. $\Delta\mathscr{E}_{pot} = \mathscr{E}_{pot}/\mathscr{E}_{pot}^0 - 1$ (the superscript '0' indicating the value at the initial time). Panel *a*) describes the global convergence achieved by halving and doubling both Δx^* and Δz^* with respect to the reference resolution. For the coarsest discretization the wave is rapidly damped because of the numerical dissipation while a good energy conservation is observed for the finest resolution (namely, $L^*/\Delta x^* = 40$, $h_0^*/\Delta z^* = 20$). The overall rate of convergence ranges between 2 and 3 according to the chosen norm. On the contrary, no convergence is observed when Δz^* is varied and Δx^* is kept constant (see panel *b*) of the same figure). This may be interpreted as a minor dependence of the depth-averaged set on Υ when a given threshold resolution over the water depth is overcome. As a consequence, the convergence rate shown in panel *c*) (where just Δx^* varies while Δz^* is constant) is practically identical to that displayed in panel *a*). The spatial discretization over the water depth is quite coarse ($h_0^*/\Delta z^* = 5$ in the coarsest case), this meaning that the proposed scheme can model the main features of wave propagation without requiring a fine resolution in the vertical direction.

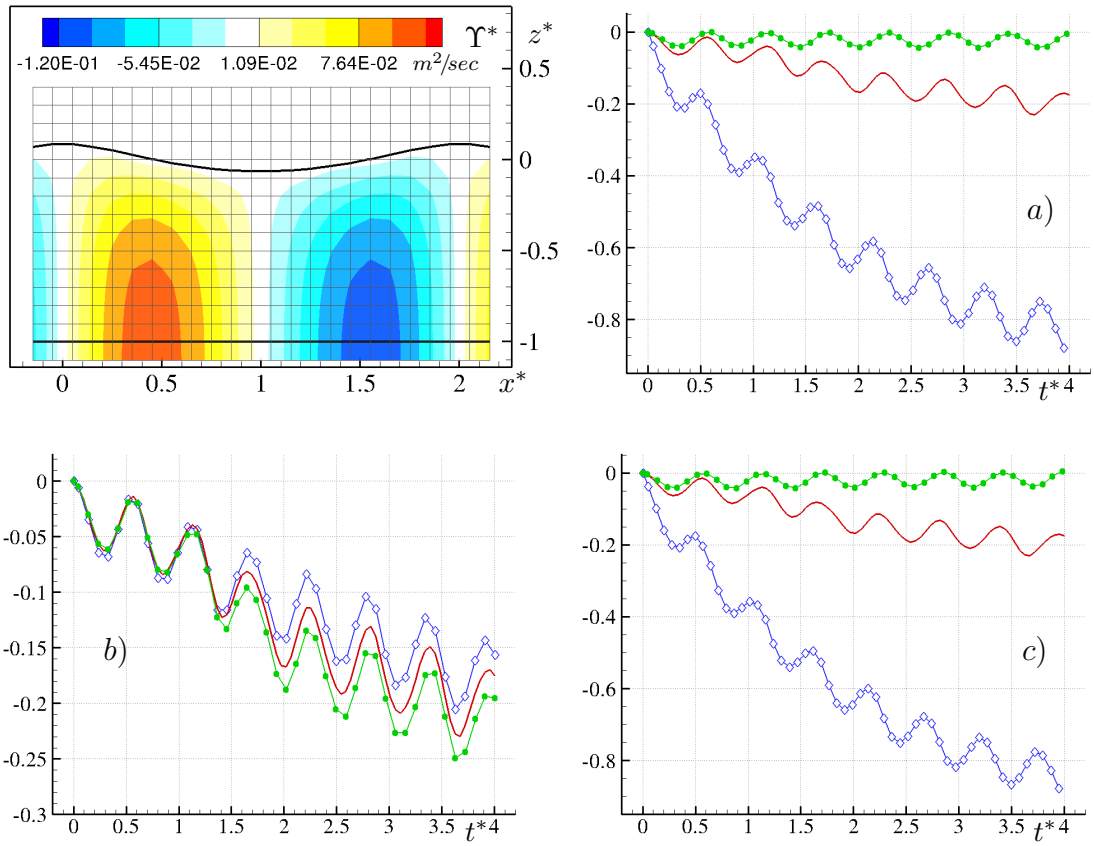

FIG. 13. The Stokes wave: case 3 of Table IV. Top left panel: sketch of the solution at the initial time for $L^*/\Delta x^* = 20$ and $h_0^*/\Delta z^* = 10$ (reference solution). Remaining panels: convergence of the global potential energy, namely $\Delta\mathscr{E}_{pot} = \mathscr{E}_{pot}/\mathscr{E}_{pot}^0 - 1$. In all panels the solid lines indicate the reference solution while the symbols '•' and '◇' denote the finest and the coarsest resolutions, respectively. Panel a): convergence by halving/doubling both Δx^* and Δz^*. Panel b): convergence by halving/doubling Δz^*. Panel c): convergence by halving/doubling Δx^*.

The propagation of Stokes waves is further investigated by running long-time simulations. Specifically, the configurations described in Table IV have been run for 30 wave periods by maintaining the ratios $L^*/\Delta x^* = 40$, $h_0^*/\Delta z^* = 20$ constant over the three cases. Specifically, each test case is characterized by the same number of points per wave length and by the same discretization along the vertical direction. This implies that the ratio $\Delta x^*/\Delta z^*$ decreases from case 1 to case 3 (see Table V). Figure 14 displays the results obtained for the free-surface elevation, η, and the generalized momentum, M (the solid lines indicate the analytical solution while the dotted lines the numerical prediction). In all the configurations (see Table IV) the numerical signals show small deviations from the theoretical profiles and display an

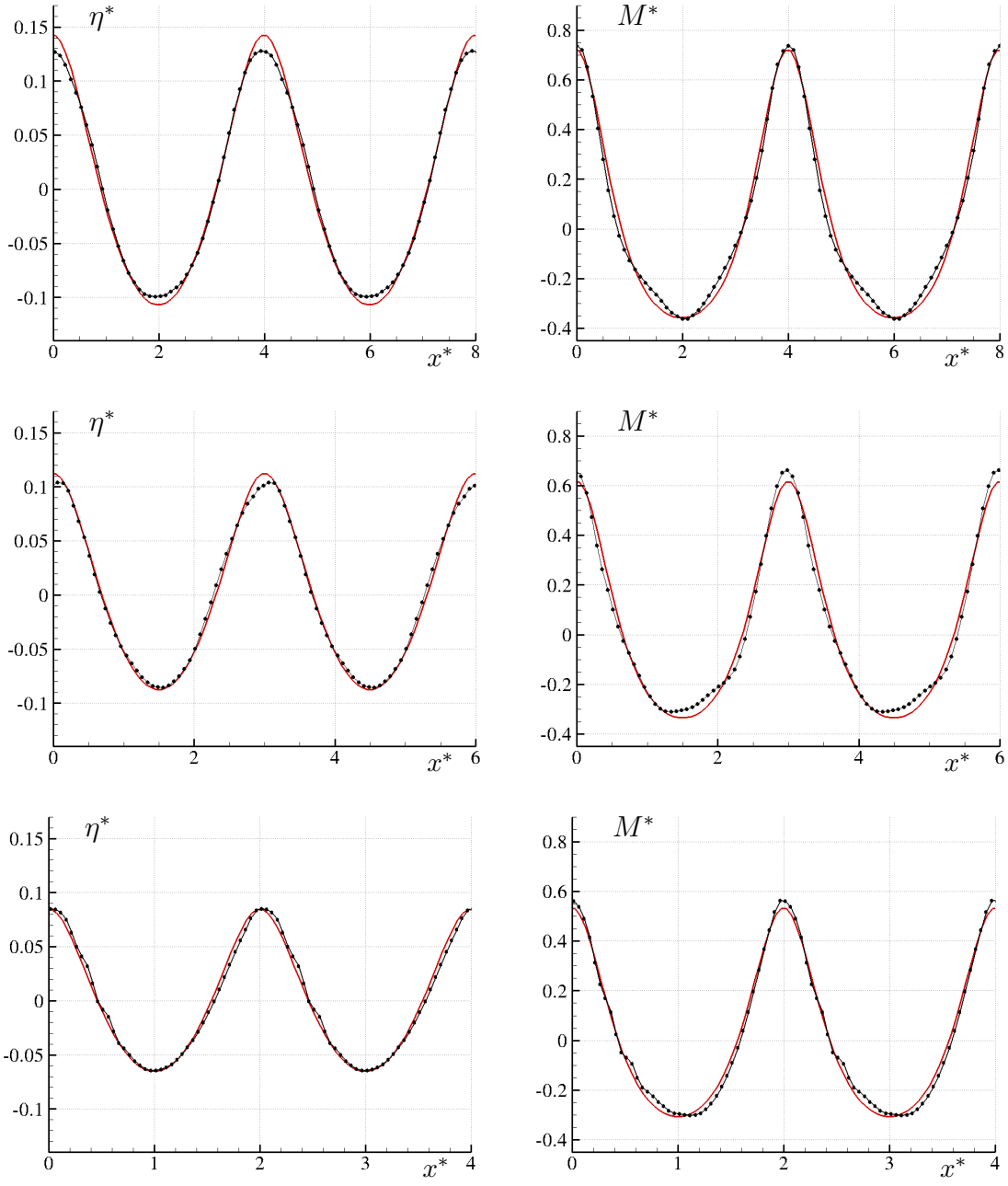

FIG. 14. The Stokes wave after 30 periods of evolution: the solid lines represent the analytical solution while the dotted lines the numerical signals. The free-surface elevation (left column) and generalized momentum (right column) for case 1 (top row), case 2 (middle row) and case 3 (bottom row) described in Table IV.

overall good agreement with the Stokes solution. For what concerns case 1 (the shallowest case), the numerical free surface appears slightly damped in comparison to the analytical one while the numerical generalized momentum correctly predicts both maxima and minima

TABLE V. Stokes waves: relative errors for the wave height (H^*) and the wave celerity (c^*) after 30 periods of evolution. The number of numerical points per wave length is the same for all the cases.

	$\Delta x^*\,(m)$	$\Delta x^*/\Delta z^*$	$L^*/\Delta x^*$	$\mathcal{E}_r\,[H^*]$	$\mathcal{E}_r\,[c^*]$
case 1	0.1	2	40	$9.17 \cdot 10^{-2}$	$7.18 \cdot 10^{-4}$
case 2	0.075	3/2	40	$4.90 \cdot 10^{-2}$	$2.15 \cdot 10^{-3}$
case 3	0.05	1	40	$1.66 \cdot 10^{-3}$	$2.44 \cdot 10^{-3}$

but, in turn, its signal appears slightly deformed, especially in the neighbourhoods of the troughs. These effects are probably due to the action of the non-linearities that, for this run, are quite large (see Table IV). Consistently, they tend to reduce as the parameter ϵ decreases (see, for example, the central panels of figure 14). Case 3 shows some small spurious oscillations both in the free-surface and generalized momentum profiles. These are likely due to the larger steepness of such a configuration (see Table IV).

As a final analysis, Table V displays the relative errors for the wave height and the wave celerity (phase velocity) for the three configurations under consideration. In the former case the error reduces as the depth increases because of the decreasing of the non-linearity parameter ϵ (see Table IV). On the contrary, the relative error for the wave celerity decreases as the water depth becomes shallower, this being a consequence of a more accurate representation of the linear dispersion relation. In any case, all the simulations above reported confirm the accuracy of the proposed scheme in describing the wave propagation and its main features (i.e. the nonlinear effects and the linear dispersion relation).

V. CONCLUSIONS

The semi-integrated model proposed by Antuono and Brocchini [1] has been reformulated in a conservative form and implemented with the two alternative Poisson equations derived by Antuono and Brocchini [1] for the vertical component of the velocity (formulation A) and for a depth semi-averaged variable, Υ (formulation B). The analysis shows that formulation A is prone to instability problems as the problem nonlinearities increase. On the contrary, formulation B allows for an accurate and robust numerical implementation.

Some relevant test cases derived from the scientific literature on Boussinesq-type models have been used to assess the proposed solution strategy and to highlight its features and characteristics. Solitary and Stokes wave solutions have been chosen as reference analytical benchmarks to inspect the ability of the proposed model in describing the propagation of waves of permanent shape in different regimes, e.g. in shallow, intermediate and in the lower bound of deep water conditions. The results confirm that the model correctly predicts the exact linear dispersion relation and the main nonlinear features of the gravity wave motion.

Shoaling properties have also been successfully validated with reference to the experimental data of Guibourg [24], also reported in Bonneton et al. [25].

The successful validation of the non-breaking model suggests that the breaking model can be safely implemented. This being underway and to be reported in a dedicated paper.

ACKNOWLEDGMENTS

This work was supported partially by the Research Council of Norway through the Centres of Excellence funding scheme AMOS, project number 223254 and partially by the Flagship Project RITMARE - The Italian Research for the Sea - coordinated by the Italian National Research Council.

Appendix A: Details of computations

In this section we show how to derive system (2) from that described in Antuono and Brocchini [1]. For the sake of simplicity, we just consider the momentum equation in the x-direction (the y-component is easily recovered by symmetry) and the Poisson equation for w along with the boundary condition in (15). Specifically, the momentum equation of the model of Antuono and Brocchini [1] is multiplied by the water depth d and, thanks to the

continuity equation, is rearranged in an almost-conservative format as follows:

$$\begin{cases} (dU)_t + \epsilon\,(dU^2)_x + \epsilon\,(dVU)_y + d\,\eta_x + \mu^2 \displaystyle\int_{-h}^{\epsilon\eta} \Upsilon_{xt}\,dz + \epsilon\,\mu^2 \int_{-h}^{\epsilon\eta} M_x^{(z)}\,dz + \\ \qquad + \mu^2 \displaystyle\int_{-h}^{\epsilon\eta} T_x^{(z)}\,dz \; + \epsilon\,M^{(x)} + \mu^2\,T^{(x)} - \tau_F^{(x)} - \tau_B^{(x)} = 0\,, \\ \mu^2\,w_{xx} \;+\; \mu^2\,w_{yy} \;+\; w_{zz} \;=\; (\,\nabla\cdot\boldsymbol{R})_z\;, \end{cases} \tag{A1}$$

where (U, V) represent the horizontal components of the depth-averaged velocity. Similarly, the local velocity field is denoted by (u, v, w). The remaining terms are given below:

$$\tau_F^{(x)} \;=\; \left[\,\epsilon\,\mu^2\,\langle\hat{u}^2\rangle\,\eta_x + \epsilon\,\mu^2\,\langle\hat{u}\hat{v}\rangle\,\eta_y - \langle\hat{u}\hat{w}\rangle\,\right]\Big|_{\epsilon\eta} \tag{A2}$$

$$\tau_B^{(x)} \;=\; \left[\,\mu^2\,\langle\hat{u}^2\rangle\,h_x + \mu^2\,\langle\hat{u}\hat{v}\rangle\,h_y + \langle\hat{u}\hat{w}\rangle\,\right]\Big|_{-h} \tag{A3}$$

$$M^{(x)} = \left[\int_{-h}^{\epsilon\eta} (\delta u)^2\,dz\right]_x + \left[\int_{-h}^{\epsilon\eta} (\delta u\,\delta v)\,dz\right]_y, \tag{A4}$$

$$T^{(x)} = \left[\int_{-h}^{\epsilon\eta} \langle\hat{u}^2\rangle\;dz\right]_x + \left[\int_{-h}^{\epsilon\eta} \langle\hat{u}\hat{v}\rangle\;dz\right]_y, \tag{A5}$$

$$M^{(z)} \;=\; \left[\int_{z}^{\epsilon\eta} uw\,d\zeta\right]_x + \left[\int_{z}^{\epsilon\eta} vw\,d\zeta\right]_y - \;w^2\,, \tag{A6}$$

$$T^{(z)} \;=\; \left[\int_{z}^{\epsilon\eta} \langle\hat{u}\hat{w}\rangle\;d\zeta\right]_x + \left[\int_{z}^{\epsilon\eta} \langle\hat{v}\hat{w}\rangle\;d\zeta\right]_y - \;\langle\hat{w}^2\rangle\;-\;\tau_F^{(z)}\,. \tag{A7}$$

Terms $M^{(x)}$ and $T^{(x)}$ directly appear in the momentum equation and are already in a conservative form. As a consequence, they are easily included in the tensor $\mathbb{F}$ of equation (6). On the contrary, more work is needed to rearrange the remaining contributions.

Let us focus on the integral of Υ_{xt}. The idea is to move the time derivative outside the integral and, then, include this term in the evolved quantity. Applying the Leibniz integral rule, it follows:

$$\int_{-h}^{\epsilon\eta} \Upsilon_{xt}\,dz \;=\; \left[\int_{-h}^{\epsilon\eta} \Upsilon_x\,\mathrm{d}z\right]_t - \;\epsilon\,\eta_t\,\Upsilon_x\big|_{\epsilon\eta} - \;h_t\,\Upsilon_x\big|_{-h}\,, \tag{A8}$$

and, using the definition of Υ in equation (3) and the Leibniz rule once again, we obtain:

$$\Upsilon_x\big|_{\epsilon\eta} \,=\, \epsilon\,\eta_x\,w\big|_{\epsilon\eta}\,, \qquad \Upsilon_x\big|_{-h} \,=\, \left[\int_{-h}^{\epsilon\eta} w\,\mathrm{d}z\right]_x \,-\, h_x\,w\big|_{-h}\,. \tag{A9}$$

Similarly, for the integral of $M_x^{(z)}$ we write:

$$\int_{-h}^{\epsilon\eta} M_x^{(z)}\,dz \,=\, \left[\int_{-h}^{\epsilon\eta} M^{(z)}\,\mathrm{d}z\right]_x \,-\, \epsilon\,\eta_x\,M^{(z)}\big|_{\epsilon\eta} \,-\, h_x\,M^{(z)}\big|_{-h}\,. \tag{A10}$$

Now, using the Leibniz formula once again, we obtain:

$$M^{(z)}\big|_{\epsilon\eta} \,=\, \epsilon\,\eta_x\,(uw)\big|_{\epsilon\eta} \,+\, \epsilon\,\eta_y\,(vw)\big|_{\epsilon\eta} \,-\, w^2\big|_{\epsilon\eta}$$

$$M^{(z)}\big|_{-h} \,=\, -\,h_x\,(uw)\big|_{-h} \,-\, h_y\,(vw)\big|_{-h} \,-\, w^2\big|_{-h} \,+\, \left[\int_{-h}^{\epsilon\eta}(uw)\,\mathrm{d}z\right]_x \,+\, \left[\int_{-h}^{\epsilon\eta}(vw)\,\mathrm{d}z\right]_y\,,$$

$$\int_{-h}^{\epsilon\eta} M^{(z)}\,\mathrm{d}z = \left[\int_{-h}^{\epsilon\eta}\mathrm{d}z\int_{z}^{\epsilon\eta}(uw)\,\mathrm{d}\zeta\right]_x \,+\, \left[\int_{-h}^{\epsilon\eta}\mathrm{d}z\int_{z}^{\epsilon\eta}(vw)\,\mathrm{d}\zeta\right]_y \,-\, \int_{-h}^{\epsilon\eta} w(uh_x + vh_y + w)\,\mathrm{d}z\,.$$

The last contribution gives term D_{ist} as defined in equation (8). The first two terms can be simplified by using the kinematic boundary conditions at the free surface and at the seabed [namely, equation (15)]. This gives:

$$M^{(z)}\big|_{\epsilon\eta} \,=\, -\,\eta_t\,w\big|_{\epsilon\eta}\,, \qquad M^{(z)}\big|_{-h} \,=\, \frac{h_t}{\epsilon}\,w\big|_{-h} \,+\, \left[\int_{-h}^{\epsilon\eta}(uw)\,\mathrm{d}z\right]_x \,+\, \left[\int_{-h}^{\epsilon\eta}(vw)\,\mathrm{d}z\right]_y$$

Collecting all the above results, we obtain:

$$\int_{-h}^{\epsilon\eta}\Upsilon_{xt}\,dz \,+\, \epsilon\int_{-h}^{\epsilon\eta} M_x^{(z)}\,dz \,=\, \left[\int_{-h}^{\epsilon\eta}\Upsilon_x\,\mathrm{d}z\right]_t \,-\, h_t\left[\int_{-h}^{\epsilon\eta} w\,\mathrm{d}z\right]_x \,+\, \epsilon\,D_{isp} \,-\, \epsilon\,h_x\,p_b\,,$$

where h_t is generally assumed to be zero while D_{isp} and p_b are defined in (8) and (12), respectively. For the integral of $T_x^{(z)}$ we follow a procedure similar to that used for the integral of $M_x^{(z)}$ and find:

$$\int_{-h}^{\epsilon\eta} T_x^{(z)}\,dz \,=\, \left[\int_{-h}^{\epsilon\eta} T^{(z)}\,\mathrm{d}z\right]_x \,-\, h_x\left[\left(\int_{-h}^{\epsilon\eta}\langle\hat{u}\hat{w}\rangle\;\mathrm{d}z\right)_x \,+\, \left(\int_{-h}^{\epsilon\eta}\langle\hat{v}\hat{w}\rangle\;\mathrm{d}z\right)_y \,-\, \tau_F^{(z)} \,-\, \tau_B^{(z)}\right]\,,$$

where the term multiplied by h_x is p_b^T while the former one can be reshaped as follows:

$$\int_{-h}^{\epsilon\eta} T^{(z)}\,\mathrm{d}z \,=\, \left[\int_{-h}^{\epsilon\eta}\mathrm{d}z\int_{z}^{\epsilon\eta}\langle\hat{u}\hat{w}\rangle\;\mathrm{d}\zeta\right]_x \,+\, \left[\int_{-h}^{\epsilon\eta}\mathrm{d}z\int_{z}^{\epsilon\eta}\langle\hat{v}\hat{w}\rangle\;\mathrm{d}\zeta\right]_y$$

$$-\int_{-h}^{\epsilon\eta}\left[\,\langle\hat{u}\hat{w}\rangle\,h_x + \langle\hat{v}\hat{w}\rangle\,h_y + \langle\hat{w}^2\rangle\,\right]\mathrm{d}z \,-\, d\,\tau_F^{(z)}\,,$$

and corresponds to D_{isp}^T. Finally, assuming $\tau_F^{(x)}$ and $\tau_F^{(z)}$ to be negligible and denoting $\tau_B^{(x)} = \tau_b$, we obtain system (2).

Appendix B: Neumann conditions for Υ

Here we derive the expressions of the Neumann conditions for Υ at the free surface and at the seabed. We start from the latter case. The normal unit vector to the seabed is:

$$\boldsymbol{n} \,=\, -\,(\,\mu\,h_x\,,\,\mu\,h_y\,,\,1\,)\,/N_h \quad \text{where} \quad N_h \,=\, \sqrt{1+\mu^2 h_x^2+\mu^2 h_y^2}\,. \tag{B1}$$

Then, the directional derivative of Υ corresponds to:

$$\frac{\partial \Upsilon}{\partial n}\Big|_{-h} \,=\, \hat{\nabla}\Upsilon\cdot\boldsymbol{n} \,=\, -\,\frac{(\,\mu^2\,\Upsilon_x\,h_x+\mu^2\,\Upsilon_y\,h_y-w\,)\,\big|_{-h}}{N_h} \tag{B2}$$

where $\hat{\nabla} \,=\, (\mu\,\partial/\partial x\,,\mu\,\partial/\partial y\,,\partial/\partial z)$. Using the gradient over the horizontal plane, namely $\nabla \,=\, (\partial/\partial x\,,\partial/\partial y)$, the above expression can be recast in the following compact form:

$$\frac{\partial \Upsilon}{\partial n}\Big|_{-h} \,=\, \hat{\nabla}\Upsilon\cdot\boldsymbol{n} \,=\, -\,\frac{(\,\mu^2\,\nabla\Upsilon\cdot\nabla h-w\,)\,\big|_{-h}}{N_h} \tag{B3}$$

Multiplying the definition of $\boldsymbol{M}$ in (3) and that of $\delta\boldsymbol{u}$ in (7) by ∇h scalarly, we find:

$$(\boldsymbol{M}-\boldsymbol{Q})\,\big|_{-h}\cdot\nabla h \,=\, \mu^2\int_{-h}^{\epsilon\eta}(\nabla\Upsilon\cdot\nabla h)\;\mathrm{d}z\,,$$

$$(\delta\boldsymbol{u}-\boldsymbol{R})\,\big|_{-h}\cdot\nabla h \,=\, -\,\mu^2\;(\nabla\Upsilon\cdot\nabla h)\,+\,\frac{\mu^2}{d}\int_{-h}^{\epsilon\eta}(\nabla\Upsilon\cdot\nabla h)\;\mathrm{d}z\,.$$

Substituting the first expression in the second one to eliminate the integral over the fluid depth, we find:

$$\mu^2\;(\nabla\Upsilon\cdot\nabla h) \,=\, \left(\frac{M}{d}+\boldsymbol{R}\big|_{-h}\right)\cdot\nabla h\,-\,\boldsymbol{u}\big|_{-h}\cdot\nabla h\,. \tag{B4}$$

Now we substitute this expression in equation (B3) and obtain:

$$\frac{\partial \Upsilon}{\partial n}\Big|_{-h} \,=\, -\,\frac{\left(\frac{M}{d}+\boldsymbol{R}\big|_{-h}\right)\cdot\nabla h\,-\,\boldsymbol{u}\big|_{-h}\cdot\nabla h-w\big|_{-h}}{N_h} \tag{B5}$$

Finally, using the expression in (15) for the kinematic boundary condition for w at the bottom, we find:

$$\frac{\partial \Upsilon}{\partial n}\Big|_{-h} \,=\, -\,\left[\,\frac{h_t}{\epsilon}\,+\,\left(\frac{M}{d}+\boldsymbol{R}\big|_{-h}\right)\cdot\nabla h\right]/N_h\,. \tag{B6}$$

Following the same procedure, it is simple to prove that:

$$\frac{\partial \Upsilon}{\partial n}\Big|_{\epsilon\eta} \,=\, -\,\left[\,\eta_t\,+\,\left(\frac{M}{d}+\boldsymbol{R}\big|_{\epsilon\eta}\right)\cdot\epsilon\nabla\eta\right]/N_\eta\,, \tag{B7}$$

where $N_\eta = \sqrt{1+\epsilon^2\mu^2\,\|\nabla\eta\|^2}$.

REFERENCES

[1]M. Antuono and M. Brocchini, "Beyond Boussinesq-type equations: Semi-integrated models for coastal dynamics," *Physics of Fluids*, vol. 25, no. 1, 2013. [Online]. Available: http://scitation.aip.org/content/aip/journal/pof2/25/1/10.1063/1.4774343

[2]I. Lakatos, *The Methodology of Scientific Research Programmes*, philosophical papers ed. Cambridge University Press, 1978, vol. 1.

[3]D. Peregrine, "Long waves on beaches," *J. Fluid Mech.*, vol. 27, no. 4, pp. 815–827, 1967.

[4]M. Brocchini, "A reasoned overview on Boussinesq-type models: the interplay between physics, mathematics and numerics," *Proceedings of the Royal Society A*, vol. 469, no. (20130496), 2013.

[5]J. T. Kirby, "Boussinesq Models and Their Application to Coastal Processes across a Wide Range of Scales," *Journal of Waterway, Port, Coastal, and Ocean Engineering*, p. 03116005, 2016. [Online]. Available: http://dx.doi.org/10.1061/(ASCE)WW.1943-5460.0000350

[6]M. Antuono, V. Liapidevskii, and M. Brocchini, "Dispersive Nonlinear Shallow Water Equations," *Stud. Appl. Maths.*, vol. 122(1), pp. 1–28, 2009.

[7]V. Casulli and G. Stelling, "Numerical simulation of 3d quasi-hydrostatic, free surface flows," *Journal of Hydraulic Engineering*, vol. 124, no. 7, pp. 678–686, 1998.

[8]M. Zijlema, G. Stelling, and P. Smit, "SWASH: An operational public domain code for simulating wave fields and rapidly varied flows in coastal waters," *Coastal Engineering*, vol. 58, pp. 992–1012, 2011.

[9]G. Ma, F. Shi, and J. Kirby, "Shock-capturing non-hydrostatic model for fully dispersive surface wave processes," *Ocean Modelling*, vol. 43-44, pp. 22–35, 2012.

[10]J. Veeramony and I. Svendsen, "The flow in surf-zone waves," *Coast. Engng.*, vol. 39, pp. 93–122, 2000.

[11]D. Cox, N. Kobayashi, and A. Okayasu, "Experimental and numerical modeling of surf zone hydrodynamics," Center for Applied Coastal Research, University of Delaware, Newark DE, U.S.A., Tech. Rep. CACR-95-07, 1995.

[12]G. Wei, J. Kirby, S. Grilli, and R. Subramanya, "A fully nonlinear Boussinesq model for surface-waves. Part 1. highly nonlinear unsteady waves," *J. Fluid Mech.*, vol. 294, pp. 71–92, 1995.

[13]F. Shi, J. T. Kirby, J. C. Harris, J. D. Geiman, and S. T. Grilli, "A high-order adptive time-stepping TVD solver for Boussinesq modelling of breaking waves and coastal inundation," *Ocean Modelling*, vol. 43-44, pp. 36–51, 2012.

[14]J. Puleo and K. Holland, "Estimating swash zone friction coefficients on a sandy beach," *Coastal engineering*, vol. 43, no. 1, pp. 25–40, 2001.

[15]E. F. Toro, *Riemann Solvers and Numerical Methods for Fluid Dynamics*, second edition ed. Springer-Verlag, 1999.

[16]——, *Shock-Capturing Methods for Free-Surface Shallow Flows*. Wiley and Sons Ltd., 2001.

[17]D.-H. Kim, P. J. Lynett, and S. A. Socolofsky, "A depth-integrated model for weakly dispersive, turbulent and rotational fluid flows," *Ocean Modelling*, vol. 27, pp. 198–214, 2009.

[18]S. Yamamoto and H. Daiguji, "Higher-order-accurate upwind schemes for solving the compressible Euler and Navier-Stokes equations," *Computers Fluids*, vol. 2, no. 3, pp. 259–270, 1993.

[19]J. Zhou, D. Causon, C. Mingham, and D. Ingram, "The Surface Gradient Method for the Treatment of Source Terms in the Shallow-Water Equations," *Journal of Computational Physics*, vol. 168, no. 1, pp. 1–25, 2001. [Online]. Available: http://www.sciencedirect.com/science/article/pii/S0021999100966701

[20]P. Amestoy and I. Duff, "Vectorization of a multiprocessor multifrontal code," *International Journal of Supercomputer Applications*, vol. 3, pp. 41–59, 1989.

[21]P. Amestoy, I. Duff, J. Koster, and J.-Y. L'Excellent, "A fully asynchronous multifrontal solver using distributed dynamic scheduling," *SIAM Journal on Matrix Analysis and Applications*, vol. 23, no. 1, pp. 15–41, 2001.

[22]Li X., Lowengrub J., Rätz A., and Voigt A., "Solving PDEs in complex geometries: a diffuse domain approach," *Communications in mathematical sciences*, vol. 7, no. 1, pp. 81–107, mar 2009. [Online]. Available: http://www.ncbi.nlm.nih.gov/pmc/articles/PMC3097555

[23]J. Fenton, "A ninth-order solution for the solitary wave," *Journal of Fluid Mechanics*, vol. 53, no. 02, pp. 257–271, 1972.

[24]S. Guibourg, "Modélisation numérique et expérimentale des houles bidimensionnelles en zone cotière," Ph.D. dissertation, Université Joseph Fourier, Grenoble, France, 1994.

[25]P. Bonneton, F. Chazel, D. Lannes, F. Marche, and M. Tissier, "A splitting approach for the fully nonlinear and weakly dispersive Green-Naghdi model," *J. Comp. Phys.*, vol. 230(4), pp. 1479–1498, 2011.

[26]B. Méhauté, *An introduction to hydrodynamics and water waves*, ser. Springer Study Edition. Springer-Verlag, 1976. [Online]. Available: https://books.google.it/books?id=G_ZQAAAAMAAJ